Determination of solid fraction–temperature relation and latent heat using full scale casting experiments: application to corrosion resistant steels and nickel based alloys

K. D. Carlson and C. Beckermann*

Casting simulation results are only useful to a foundry if they reflect reality, which requires accurate material datasets for the alloys being simulated. Material datasets include property data such as density, specific heat and thermal conductivity as functions of temperature, as well as latent heat of solidification and a solid fraction–temperature relation. Unfortunately, there are a significant number of commonly used metal alloys for which no reliable material data are available. The present study focuses on five such corrosion resistant alloys: superaustenitic stainless steel CN3MN, duplex stainless steels CD3MN and CD4MCuN and nickel based alloys CW6MC and N3M. Initial alloy material datasets are generated using thermodynamic simulation software. Comparisons of temperatures measured in full scale sand castings made from these alloys with temperatures predicted in computer simulations revealed that these initial datasets are inadequate. Therefore, an iterative method is developed to adjust the datasets (in particular the solid fraction–temperature relation and latent heat) in order to match measured and predicted temperatures and cooling rates. Uncertainties in the simulation are effectively eliminated through parametric studies. Although more tedious, the present iterative method to determine the solid fraction–temperature relation and latent heat is believed to be more accurate than traditional cooling curve analysis using small experimental castings.

Keywords: Casting simulation, Temperature measurements, Solid fraction, Latent heat, Stainless steels, Nickel based alloys

Introduction

Casting simulation is routinely used in modern foundries because many casting problems can be predicted and eliminated through the use of simulation rather than through time consuming and potentially expensive trial and error casting production. An important caveat for casting simulation, however, is that the results from a simulation are only as good as the casting data that are utilised in the simulation; for a simulation to truly reflect reality, it is necessary to have material datasets that accurately characterise the materials being simulated. These material datasets include property data such as density, specific heat and thermal conductivity for all materials involved (e.g. metal alloy, mould, core materials, etc.) as well as the latent heat of solidification of the alloy and the alloy's solid fraction–temperature relationship for a cooling rate representative of the process being modelled. It is also necessary to have reasonably accurate boundary and initial conditions. Adequate material datasets have been developed for many common casting alloys and mould materials based on a wealth of experimental data that have been gathered in the last half century. However, for many less common or newer alloys, little or no material data are available, and hence, accurate simulation of castings made from these alloys is not possible. One group of alloys for which little material data are available is corrosion resistant alloys required for severe service conditions (e.g. high temperature, high pressure, involving corrosive fluids, etc.). Castings made from these alloys are commonly employed, for example, in the petroleum industry. This investigation focuses on five corrosion resistant alloys, which were selected by polling foundries that produce castings for severe service regarding the alloys that they most commonly use for which material data are not currently available. The alloys selected consist of three stainless steels (superaustenitic CN3MN and duplexes CD3MN and CD4MCuN) and two nickel based alloys (CW6MC and N3M). The compositions of these alloys from the casting experiments performed for the present study are given in Table 1.

Department of Mechanical and Industrial Engineering, The University of Iowa, Iowa City, IA 52242, USA

*Corresponding author, email becker@engineering.uiowa.edu

Received 13 April 2011; accepted 26 August 2011
DOI 10.1179/1743133611Y.0000000023

The quickest, simplest way to develop material datasets is to utilise thermodynamic simulation software packages. Using information from thermodynamic databases, these packages model multicomponent metal alloy solidification to generate a solidification path. The solidification path consists of mass fractions and compositions of the various solid phases that form as a function of temperature during solidification. This information is then used to determine the latent heat and temperature dependent data for the specific heat and density. Two different thermodynamic simulation software packages are utilised in the present study: the stainless steels are simulated using the interdendritic solidification package IDS (IDS DOS v2·0·0) developed by Miettinen[1] and Miettinen and Louhenkilpi,[2] and the nickel based alloys are simulated using JMatPro.[3] Many such software packages are commercially available; these two were selected in part because in addition to generating a solidification path and thermodynamic properties, they also produce transport property curves (i.e. thermal conductivity and viscosity) required by casting simulation software. IDS is only applicable to steels, whereas JMatPro can be applied to a wider range of alloys (including nickel based alloys). IDS calculates the transient diffusion of solutes within the phases on the scale of the microstructure and is thus able to account for the effect of back diffusion on the solidification path and to simulate the solid state transformations that often occur in steels. JMatPro, on the other hand, uses a modified Scheil approximation (i.e. no solute diffusion in solid phases, except for carbon and nitrogen, for which diffusion in the solid is assumed to be complete).

For many common casting alloys, the datasets generated by thermodynamic software packages are reasonably accurate. However, for the highly alloyed metals considered in the present study, material datasets determined from thermodynamic simulation software are not entirely trustworthy. Sometimes, the content of a particular solute is simply out of the range for which the software was designed, or the thermodynamic database on which the software is based is not fully validated for very high solute contents. More often, the accuracy of the modified Scheil approximation or even the diffusion calculations is not known. This uncertainty affects primarily the solidification path (although the term 'solidification path' broadly includes mass fractions and compositions of all solid phases that form during solidification, the term is frequently used in a narrower sense in this text, as shorthand notation to refer simply to the solid fraction as a function of temperature, which is the only part of the broader set of information utilized in casting simulation software) and the evolution of latent heat; the specific heat, density, thermal conductivity and viscosity are generally less sensitive to potential inaccuracies in the predictions of the thermodynamic software. In order to generate reliable material datasets for the corrosion resistant alloys currently of interest, it is necessary to collect temperature data that can be used to verify the calculated solidification path and enthalpy related properties for these alloys. Note that although it is commonly referred to as a property, the solidification path is, in reality, a function of the cooling rate. Thus, it would be advantageous to determine the solidification path for cooling rates similar to those seen in production castings.

There are two common laboratory methods for measuring solidification and enthalpy related properties: differential thermal analysis (DTA) and differential scanning calorimetry (DSC). In DTA, thermocouples (TCs) are used to measure temperature differences during the heating or cooling of a small (~200 mg) sample of a metal alloy.[4] The nature of these temperature changes indicates different events that occur during solidification and melting. The DSC approach is similar to DTA, but differences in heat flow are measured rather than temperature differences. Measurements from DTA and DSC can provide a great deal of useful information for metal alloys.[4] However, while the liquidus temperature and the latent heat can be readily determined with these methods, the non-equilibrium solidus temperature is potentially more elusive. As noted in Ref. 4, determination of the solidus temperature [in the following, the term 'solidus temperature' is used as shorthand notation to indicate the (non-equilibrium solidus) temperature at which an alloy becomes fully solid upon cooling.] can be difficult with DSC/DTA. This is particularly true for alloys like steel, where the end of solidification is not associated with the formation of a new phase (e.g. a eutectic phase). In addition, the solidus temperatures of steels are generally a strong function of the cooling rate, and cooling rates during solidification

Table 1 Casting experiment alloy compositions/wt-%

	Alloy				
	Stainless steels			Nickel based alloys	
Element	(Superaustenitic) CN3MN	(Duplex) CD3MN	(Duplex) CD4MCuN	CW6MC	N3M
C	0·03	0·02	0·022	0·01	0·004
Mn	0·54	1·01	0·76	0·72	0·64
Si	0·81	0·64	0·59	0·71	0·23
P	0·005	0·018	0·02	0·009	0·007
S	0·01	0·006	0·001	0·001	0·0001
Cr	20·32	22·1	25·7	21·56	0·3
Ni	25·07	6·35	5·76	60·68 (balance)	66·84 (balance)
Mo	6·41	2·56	1·84	9·1	31·0
Cu			3·0		
Cb/Nb				3·73	
Fe	46·57 (balance)	67·16 (balance)	62·16 (balance)	3·48	0·98
N	0·24	0·14	0·15		

of castings are highly variable and often unknown. Therefore, selecting a representative cooling rate to use in DSC/DTA measurements can be a challenge. Commercial DSC/DTA systems may not even allow for tests to be conducted at the cooling rates encountered in production castings. Finally, it is difficult to back out the full solid fraction versus temperature relationship from DSC/DTA measurements.

Solidification characteristics such as the liquidus and solidus temperatures, the latent heat of solidification and the solidification path can also be determined using data from TCs embedded in small experimental castings. This method is referred to as cooling curve analysis (CCA).[5–10] Taking the time derivative of a measured temperature curve $T(t)$ yields the cooling rate curve $\mathrm{d}T/\mathrm{d}t$. The liquidus and solidus temperatures are taken directly from this cooling rate curve; this will be discussed in detail later. Two methods are commonly used to determine the latent heat of solidification and the solidification path: Newtonian analysis[5] and Fourier analysis.[6] These methods are briefly reviewed here; more detailed descriptions are provided in Refs. 5–10. A noteworthy early example of CCA can be found in Ref. 11, which provides results of an extensive experimental study performed in the 1970s, involving >40 different steel alloys. For each alloy, the liquidus temperature, solidus temperature and solid fraction versus temperature relationship were determined for a variety of cooling rates.

In Newtonian analysis, metal temperature measurements are taken using a single TC in the casting cavity of a small cylindrical cup. The casting sample in which the TC resides must be small (typically a few centimetres in both diameter and height), because Newtonian analysis is based on the lumped capacitance method, which assumes that the sample temperature is uniform. It is further assumed that both the density and specific heat of the metal are constant. In Newtonian analysis, a smooth curve is fitted to the cooling rate data to connect the cooling rate curves before and after solidification, producing a fictitious cooling rate curve termed the Newtonian zero curve, which represents the cooling rate curve if no phase change were to take place. The latent heat is then estimated by integrating over time the area between the measured cooling rate curve and the Newtonian zero curve. The fraction solid at any time [and hence temperature, since $T(t)$ is known from measurements] during solidification can then be evaluated by dividing the cumulative area between the cooling rate curve and the Newtonian zero curve up to that time by the total latent heat. The approximate nature of the results derived from this method stems primarily from the uncertainty associated with generating the Newtonian zero curve.[7,8] However, a more systematic methodology for determining the Newtonian zero curve was developed in Ref. 9. While the Newtonian method is often used for aluminium alloys, the uniform temperature assumption makes this method less practical for steel and nickel based alloys, which have substantially lower thermal conductivity than aluminium alloys. In addition, the small sample size can lead to cooling rates that are different from those encountered in production castings.

Fourier analysis[6] is similar to Newtonian analysis, but Fourier analysis requires less restrictive assumptions. Again, casting experiments are performed using a small cylindrical sample in a cup. In contrast to Newtonian analysis, Fourier analysis does not assume a uniform temperature but accounts for heat conduction within the solidifying metal. This requires knowledge of the temperature distribution in the casting sample, which is gained using two TCs in the metal rather than one: in addition to a central TC, there is also a TC located near the edge of the cylinder. An energy balance then provides an equation for $\mathrm{d}T/\mathrm{d}t$ in terms of a conduction term and a latent heat source term. Assuming that heat transfer in the cylindrical sample occurs only radially, with no heat transfer from the cylinder ends, the time dependent value of the conduction term is determined from an analytical expression involving the measured temperatures. This conduction term is then designated the Fourier zero curve, which serves the same purpose as the Newtonian zero curve. The Fourier zero curve can be expected to be more accurate than the Newtonian zero curve, but it is still only approximate. The analytical expression used for the conduction term assumes not only a one-dimensional system but also time independent, steady conduction without heat generation (something that is rarely mentioned). None of these assumptions are true in reality, and using time dependent (measured) temperatures in an analytical expression that is strictly only valid for steady conduction does not necessarily compensate for any errors. Analogous to Newtonian analysis, the latent heat and solidification path can be determined by integrating the difference between the measured cooling rate curve and the Fourier zero curve. This solution requires iteration, because in Fourier analysis, both the thermal diffusivity and the volumetric specific heat are taken as functions of the solid fraction in the solidification range, and so they need to be determined as part of the solution. Results generated for aluminium alloys using both Newtonian and Fourier analyses are reviewed and compared by Barlow and Stefanescu[7] as well as by Emadi and Whiting[8] and Emadi *et al.*[10] Not surprisingly, these studies conclude that the latent heat values determined using Fourier analysis agree better with the values obtained from other methods, including DSC.

In the present study, to determine the material datasets for five corrosion resistant steel and nickel based alloys, a different approach is used, which involves a combination of full scale casting experiments and casting computer simulation. Temperature measurements are taken in the castings as they solidify and cool. These measurements immediately yield the liquidus and solidus temperatures. However, instead of constructing a zero curve, the solidification path and latent heat are obtained in a trial and error procedure, where measured and predicted temperatures and cooling rates are compared, and the material dataset is adjusted until good agreement is obtained. The initial material dataset is generated with thermodynamic software. The present iterative method does not require any of the approximations associated with the generation of a zero curve, and it is made feasible by the fact that the casting solidification simulations (excluding filling) require <10 min of run time, so many iterations can be performed if necessary. It is true that casting simulations can have errors associated with them, particularly in the choice of the simulation parameters for the pouring

temperature and the interfacial heat transfer coefficients (IHTCs) between the metal and the mould, but steps are taken in the present study to eliminate the uncertainties associated with these parameters. Material datasets are developed for the corrosion resistant alloys CN3MN, CD3MN, CD4MCuN, CW6MC and N3M. These are all highly alloyed metals, rendering datasets created from thermodynamic simulation alone uncertain. The castings in which TCs are embedded for this study are plates with a thickness that is commonly encountered in foundries casting these alloys, such that the data collected in these experiments are representative of typical cooling rates seen in production castings.

It is worth noting that the comparisons between measured and simulated temperature data, utilised in the present work to develop accurate material datasets, have value in and of themselves. While casting simulation is performed routinely, detailed comparisons between measured and predicted temperatures in an actual casting are scarce in the open literature. Issues such as the selection of simulation parameters (e.g. pouring temperature and mould/metal IHTC) are often discussed among simulation users but are not investigated systematically, as in the present study. A thorough investigation into the effects of the simulation parameters is necessary, since they are generally unknown and their choice will affect the determination of alloy properties.

In the next section, an overview is given of the data that must be input into the casting simulations, which includes a brief discussion of the accuracy of these data. The section entitled 'Casting experiments and measurement uncertainty' discusses the casting experiments that were performed for this study, and the section entitled 'Determining characteristic temperatures from TC data' describes how characteristic temperature data were determined from the temperature measurements collected during the casting experiments. The section entitled 'Solidification path and thermophysical properties' then details how the alloy material datasets were generated and modified based on the TC data. A comparison of the liquidus, solidus and latent heat values determined in the present study with those predicted by the thermodynamic simulation software is provided in the section entitled 'Comparison between measured values and thermodynamic simulation values'.

Casting simulation input

Since the present study is concerned with developing material datasets for casting simulation, it is useful to briefly review the governing equations being solved and the input required. All commercial casting simulation software packages are capable of modelling the melt flow during filling of the mould and the heat transfer during the entire casting process. Filling is simulated by solving the relevant fluid flow equations for the liquid metal as it enters the mould, which requires knowledge of the density and viscosity of the liquid metal. In addition, energy balance equations are solved in both the metal and the mould during filling. Solidification during filling is typically neglected. The solution of the energy equations requires knowledge of the densities, specific heats and thermal conductivities of the materials involved, all as a function of temperature. In the present study, all mould properties are taken from material databases supplied with the simulation software (*see* below).

When filling is complete, solidification and cooling of the casting are simulated. This also involves solving energy balance equations in both the metal and the mould but typically neglects the effect of heat advection by the residual flow of the liquid metal in the mould cavity. Then, the energy equation for the metal, after completion of filling, can be expressed as

$$\bar{\rho}\left(\bar{c}-L_{\mathrm{f}}\frac{\mathrm{d}f_{\mathrm{s}}}{\mathrm{d}T}\right)\frac{\partial T}{\partial t}=\nabla\cdot\left(\bar{k}\nabla T\right) \tag{1}$$

where T is the metal temperature, t is the time and f_{s} is the solid mass fraction (i.e. $f_{\mathrm{s}}=0$ if the metal is locally all liquid, and $f_{\mathrm{s}}=1$ if it is all solid). The use of the total derivative in the term $\mathrm{d}f_{\mathrm{s}}/\mathrm{d}T$ implies that the solid fraction is assumed to be a function of temperature only. The density, specific heat and thermal conductivity of the metal are denoted by $\bar{\rho}$, $\bar{c}$ and $\bar{k}$ respectively. The overbar is used to emphasise that these properties are mixture quantities that depend on the amount of each phase present, in addition to temperature. The term L_{f} represents the latent heat of fusion per unit mass, which is assumed to be constant over the solidification temperature range. The quantity in brackets on the left side of equation (1) has two terms: the first term accounts for the sensible heat, and the second accounts for the latent heat. This bracketed quantity is often referred to as the effective specific heat, i.e.

$$c_{\mathrm{eff}}=\bar{c}-L_{\mathrm{f}}\frac{\mathrm{d}f_{\mathrm{s}}}{\mathrm{d}T} \tag{2}$$

Note that the latent heat term in equation (2) is only non-zero while solidification is occurring, since $\mathrm{d}f_{\mathrm{s}}/\mathrm{d}T=0$ in fully liquid and completely solidified metal. The negative sign in equation (2) is the result of $\mathrm{d}f_{\mathrm{s}}/\mathrm{d}T$ being negative during solidification; the release of latent heat generally increases the effective specific heat. All of the metal alloy properties required for casting simulation, as well as the solidification path, are generated by thermodynamic simulation software packages. The predicted values for the density, thermal conductivity and, for the most part, specific heat are assumed to be reasonably accurate. The focus in the present study is on verifying and improving the accuracy of the solidification path and the latent heat predicted by the thermodynamic software.

In addition to supplying material datasets for the simulation, it is also necessary to provide initial temperatures for the metal and the mould. The initial mould temperature is easily determined from sand TC data, but the initial metal temperature (i.e. the simulation pouring temperature) is generally not well known. The simulation pouring temperature represents the temperature of the metal stream as it enters the mould cavity. Typically, temperatures are taken in the furnace, and the metal temperature drop going from the furnace to the ladle to the mould is estimated by a rule of thumb. Even if a temperature measurement is taken in the ladle immediately before pouring, the metal stream cools significantly before it reaches the mould cavity. However, by comparing measured metal temperature readings with corresponding simulated values, it is possible to determine the correct simulation pouring temperature. This will be explained in

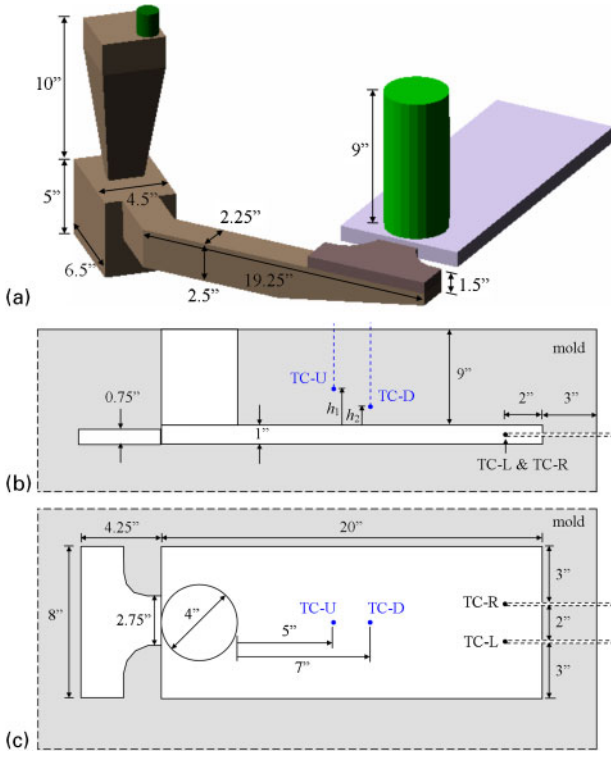

a isometric view; *b* side view, no gating except ingate; *c* top view, no gating except ingate

1 Schematics of rigging and TC arrangement for plate casting experiments: dashed lines at mould edges indicate mould continues past dashed line

the section entitled 'Solidification path and thermophysical properties'.

Finally, to solve the governing equations for fluid flow and heat transfer in a casting simulation, it is necessary to provide boundary conditions. The average flow rate of the metal entering the mould is determined from the metal inlet area and the total pouring time. The heat transfers between the mould and the environment and between the top of the riser and the environment are modelled using default settings in the casting simulation software utilised in the present study; the default mould/environment heat transfer boundary condition assumes natural convection, and the default riser top/environment boundary condition assumes hot topping is used, and that heat transfer occurs due to natural convection and radiation. Both of these boundary conditions are reasonable (and have a relatively minor effect on the present results). The most important boundary condition that must be specified is the mould/metal IHTC. The choice of the IHTC used in the present study is investigated in detail in the section entitled 'Solidification path and thermophysical properties'.

Casting experiments and measurement uncertainty

In the casting experiments, two $1 \times 8 \times 20$ in. ($2{\cdot}54 \times 20{\cdot}32 \times 50{\cdot}8$ cm) plates were cast from each alloy (*see* Table 1), with one plate cast per mould. For each alloy, the plates were poured sequentially from the same heat and ladle. The 1 in. (2·54 cm) plate thickness was selected because it is a typical section size for castings made from these alloys. The plates were end gated beneath a 4 in. (10·2 cm) diameter end riser. A schematic of the casting configuration is shown in Fig. 1. The moulds were all made from phenolic urethane no bake sand. However, there was one notable addition: in the CD3MN moulds, there was a layer of chromite sand ~1 in. (2·54 cm) thick surrounding the plate. This is a standard practice for this alloy at the casting foundry, so it was automatically performed when the mould was made, even though it was not requested.

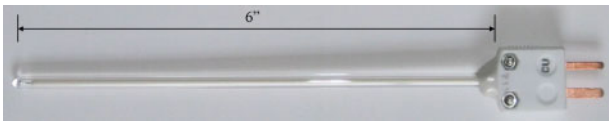

2 Photograph of one of 0·157 in. (4 mm) o.d. B type TCs employed in present study

In each mould, temperature measurements were made using two K type TCs in the sand (TC-U and TC-D in Fig. 1) and two B type (Pt–6%Rh/Pt–30%Rh) TCs in the plate (TC-L and TC-R in Fig. 1). The heights above the plate of the K type TCs, i.e. h_1 and h_2, were targeted to be 2 in. (5·08 cm) and 1 in. (2·54 cm) respectively; the actual heights, which varied somewhat, were recorded so that the virtual TCs in the simulations would be in the correct locations. The B type TCs were constructed by encasing 0·010 in. (0·254 mm) diameter B type TC wires in a two-hole alumina ceramic tube and then inserting this assembly into a 6 in. (15·2 cm) long closed end fused quartz tube with a wall thickness of 1 mm. The TC junction was in contact with the inside wall of the quartz tube at the closed end. Most of the B type TCs utilised quartz tubing with an outer diameter (o.d.) of 0·236 in. (6 mm), but three TCs used 0·157 in. (4 mm) o.d. quartz tubing. The three smaller o.d. TCs, which have a somewhat faster response time than the larger o.d. TCs, were created to determine whether or not such small diameter TCs would endure the filling and solidification process. A photograph of one of the 0·157 in. (4 mm) o.d. TCs is shown in Fig. 2. The K and B type TCs were connected to a PersonalDaq/3005 (Ref. 12) portable data acquisition system running DASYLab[13] data acquisition software. The data acquisition rate utilised for the temperature measurements was 3 Hz. The resulting temperature curves were smoothed using a nine-point moving average. Cooling rate curves were derived from these smoothed temperature curves using a central difference approximation of the time derivative. Finally, nine-point smoothing was applied to the cooling rate curves as well.

The casting experiments were very successful in that none of the 20 B type TCs failed during data acquisition (which is a vast improvement over the 25% failure rate the present authors encountered in a previous set of casting experiments).[14] In particular, all of the 0·157 in. (4 mm) o.d. TCs survived, indicating that such small TCs are indeed a viable option for such experiments. Note that the TCs in the present study were intentionally oriented such that during filling, the inflowing metal would meet the TCs 'head on' at the minimum TC cross-section. If the TCs were oriented such that the inflowing metal stream met a significant length of the quartz tube in cross-flow, for example, then it is possible that the force of the metal wave could break the TCs.

An example of the temperature versus time curves generated from the TC data is shown in Fig. 3*a* for

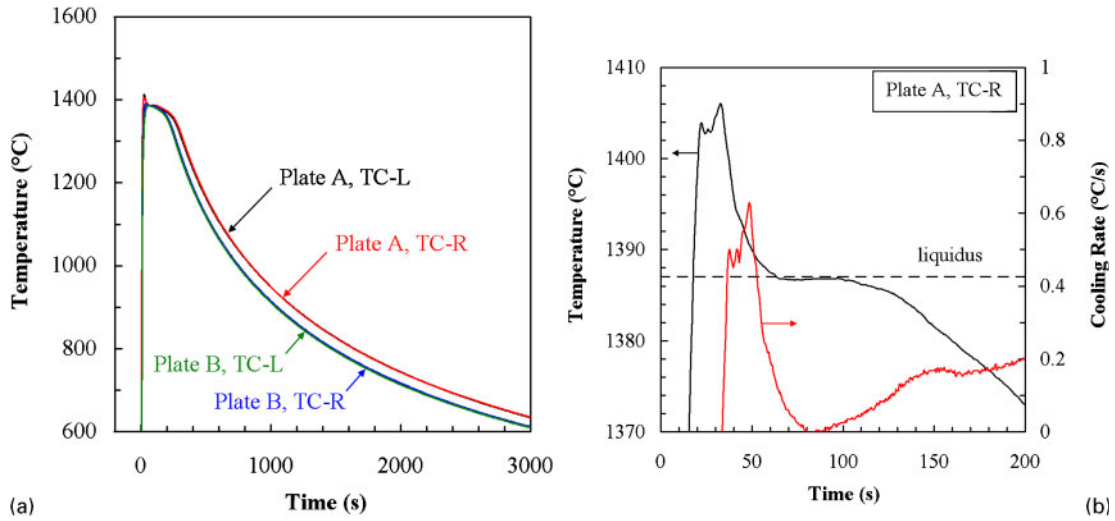

a temperature measurements for both CN3MN plates; *b* temperature and cooling rate curves near liquidus for TC-R in plate A

3 CN3MN TC results

CN3MN. The two plates are denoted as 'A' and 'B'. Note the excellent agreement between the two TCs in each plate. The difference in temperatures between the two plates during cooling is the result of the difference in the pouring temperature for each plate, which leads to slightly different cooling rates. Figure 3*a* is a representative result from the casting experiments; similar TC agreement was seen for all alloys studied.

The uncertainty in the temperature measurements can be quantified as follows. The maximum error of the B type TCs is stated by the manufacturer[15] as 0·5% $^{\circ}C^{-1}$. This translates to a maximum error of $\pm 7^{\circ}C$ at 1400°C. The relatively large size of the TC assembly requires careful consideration of the thermal lag. The dynamic response of the 6 mm o.d. TCs was evaluated by analysing the initial, rapid temperature increase associated with the liquid metal coming into contact with the TC (*see* Fig. 3*a*). Assuming that the TC assembly experiences a step change in the environment temperature (from room temperature to the liquid metal temperature), and treating the TC junction as a lumped capacitance, the TC temperature can be expected to increase exponentially. Then, the thermal time constant τ is given by the time it takes the TC to reach 63·2% (=1–1/*e*) of the environment temperature (i.e. the liquid metal temperature). Using this method, the time constant of the 6 mm o.d. TCs was determined from the temperature measurements shown in Fig. 3 to be $\tau=3$ s. During cooling, the environment temperature does not experience a step change but can be approximated as decreasing linearly at a given cooling rate. Performing another lumped capacitance analysis using this constant cooling rate assumption, it can be shown that the maximum temperature lag of the TC is then given by $\Delta T_{lag}=\tau|dT/dt|$. As shown below, the maximum cooling rates in the present experiments are in the order of 1°C s^{-1}. Hence, the maximum temperature lag during cooling is estimated to be $\Delta T_{lag}=3^{\circ}C$. It is true that the time constant could be different during heating and cooling of the TC, but considering that the thermal resistance between the TC junction and the metal is dominated by the contact resistance between the junction and the quartz tube and the conduction resistance through the quartz tube wall, the difference will be small.

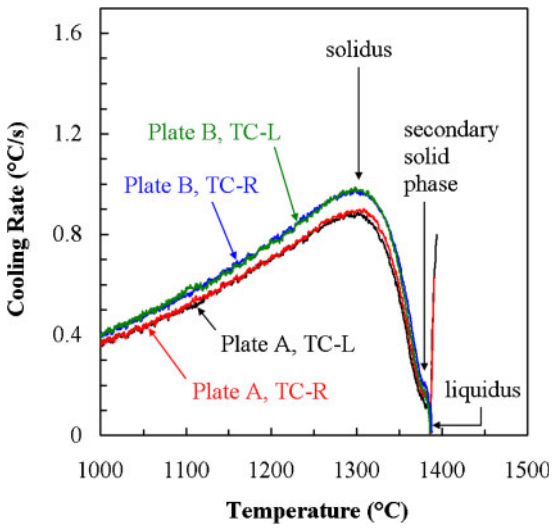

4 Cooling rate versus temperature for all four CN3MN TCs

Determining characteristic temperatures from TC data

Taking the time derivative of the temperature curves shown in Fig. 3*a* produces corresponding cooling rate versus time curves for each TC. As discussed below, cooling rate data can be used to identify different events that occur during solidification and cooling. Rather than plotting both temperature and cooling rate as functions of time, time can be eliminated from consideration, and the cooling rate can simply be plotted as a function of temperature, as shown for CN3MN in Fig. 4. Note in this figure that the cooling rate is defined as $-dT/dt$, such that decreasing temperature with time produces positive values. Eliminating time from Fig. 4 is an important feature in the present method because it clearly illustrates the temperatures at which different features in the cooling rate curves occur. Eliminating time also allows multiple experiments to be compared more readily than if the data are presented as a function

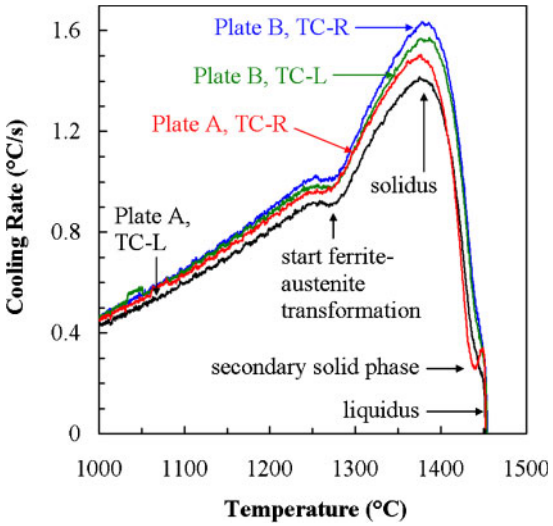

5 Cooling rate versus temperature for all four CD3MN TCs

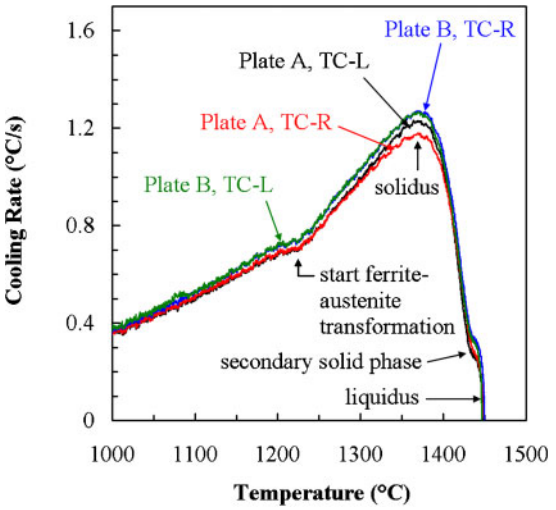

6 Cooling rate versus temperature for all four CD4MCuN TCs

of time, even in the present case where the cooling rate varies slightly from TC to TC.

The liquidus temperature is associated with the sharp minimum in Fig. 4, where the cooling rate is near zero. This can be better seen in Fig. 3*b*, where the measured temperature and cooling rate near the liquidus are plotted on a very fine scale. There is a period of >30 s where the temperature is constant to within ~0·5°C. This temperature plateau best represents the liquidus, since there is almost no recalescence. Recalescence is associated with the temperature experiencing a pronounced minimum (indicating the maximum liquid undercooling and the end of nucleation) before reaching a plateau. The absence of such a minimum in the present measurements, at least to within 0·5°C, indicates that nucleation occurs very near the equilibrium liquidus temperature without significant liquid undercooling. Of course, in the presence of recalescence, the plateau temperature does not represent the liquidus temperature. However, in the absence of any appreciable recalescence, the plateau temperature does closely correspond to the liquidus temperature. In addition, note that thermal lag of the TCs does not play a role in the present liquidus temperature measurements.

Below the liquidus temperature, the cooling rate begins to rise as solidification proceeds. The cooling rate reaches a maximum at the solidus temperature T_{sol}, when solidification is complete and the release of latent heat terminates. The solidus temperature is also indicated in Fig. 4. Note that the solidus temperature is easily distinguished in Fig. 4. This is very straightforward compared with DTA/DSC, even for the present alloys where there is very little latent heat released at the end of solidification. Any kinks in the cooling rate curve between liquidus and solidus indicate the formation of additional solid phases. A secondary solid phase is seen in Fig. 4, where there is a small inflection in the curves near the liquidus temperature. This may indicate the formation of carbides. Note that there is good agreement among all four TCs in the values of the characteristic temperatures; a similar agreement is seen for the other alloys as well, lending validity to the characteristic temperature values. In addition, note in Fig. 4 that although the two plates ('A' and 'B') had slightly different cooling rates due to the difference in the pouring temperatures, the characteristic temperatures are still in close agreement.

The measured cooling rate versus temperature curves for the two duplex stainless steels (CD3MN and CD4MCuN) are given in Figs. 5 and 6. Again, the liquidus temperature is indicated by a vanishing cooling rate. In addition, a secondary solid phase is seen to form during solidification, just below the liquidus temperature. The solidus temperatures can also be easily identified. In addition, Figs. 5 and 6 also show a characteristic temperature that did not occur in Fig. 4. Unlike CN3MN, which solidifies as austenite and remains austenite down to room temperature, the duplex steels solidify as ferrite, and then at some temperature below solidus, about half of the ferrite begins to undergo a solid state transformation into austenite. The ~50% ferrite–50% austenite final structure is why these stainless steels are termed 'duplex'. The latent heat release associated with the beginning of the ferrite to austenite phase change causes a local minimum (or at least a significant inflection point) in the cooling rate curves; this is denoted in Figs. 5 and 6. The end of this transformation is subtle enough that it cannot be reliably detected in the cooling rate curves.

The measured cooling rate versus temperature curves for the two nickel based alloys are shown in Figs. 7 and 8. Note that the cooling rate scale in these figures is different from the scale used for steels, because the cooling rates in the nickel based alloys are smaller than in the steels. As with CN3MN, the liquidus for these two alloys corresponds to the point where the cooling rate vanishes, and the maximum in the cooling rate below liquidus denotes the solidus. As with the steels, a secondary solid phase forms during solidification, just below the liquidus temperature. However, for the two nickel based alloys, a third solid phase is also observed to form during solidification. This tertiary solid phase causes a relatively pronounced and sharp local minimum in the cooling rate curves for CW6MC (*see* Fig. 7), and it causes an additional inflection in the cooling rate curve for N3M (*see* Fig. 8).

The characteristic solidification and phase transformation temperatures denoted in Figs. 4–8 are summarised in Table 2. The latent heat values in the rightmost column of

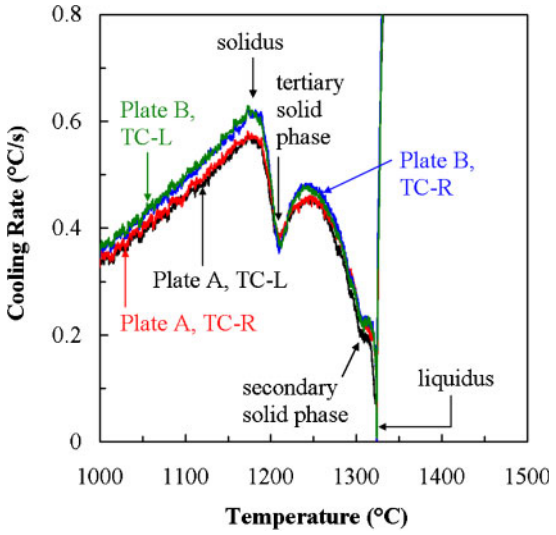

7 Cooling rate versus temperature for all four CW6MC TCs

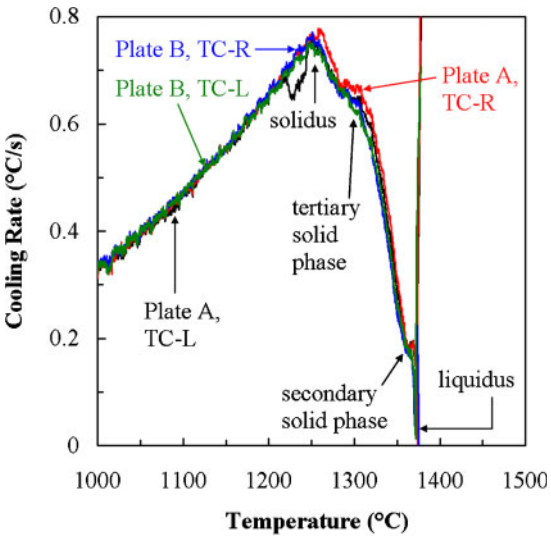

8 Cooling rate versus temperature for all four N3M TCs

Table 2 were determined in conjunction with simulation and will be addressed in the next section. The variation associated with each temperature given in Table 2 indicates the variability of these values among the four TCs for each alloy. For the 20 characteristic temperatures given in Table 2, the average variation is ± 3°C, with no variation being larger than ± 5°C. Thus, the measurements can be considered highly reproducible, despite being performed in a foundry setting. Note that this variation is of the same magnitude as the thermal lag estimated in the previous section. Hence, the characteristic temperatures can be considered quite accurate.

Solidification path and thermophysical properties

Thermodynamic simulation and casting simulation details

Initial material datasets were generated for each alloy using the compositions listed in Table 1. IDS[1,2] was used for the three steels (CN3MN, CD3MN and CD4MCuN). It should be noted that due to the high alloying contents in these steels, two of these alloys had elemental compositions that exceed the recommended IDS ranges. The CD4MCuN copper content (3%Cu) exceeds the recommended IDS range of 0–1%. The CN3MN nickel content (25·07%Ni) exceeds the IDS range of 0–16%, and the CN3MN molybdenum content (6·41%Mo) exceeds the IDS range of 0–4%. The recommended ranges given by IDS indicate ranges of alloying elements over which the thermodynamic databases utilised by IDS were developed. Extrapolation errors may occur when IDS ranges are exceeded. Because IDS accounts for finite rate solute diffusion, it is necessary to provide information regarding the cooling rate as a function of temperature. This was performed using the data shown in Figs. 4–6. On each of these cooling rate versus temperature plots, vertical lines were drawn across the plots to create five to eight temperature zones, and the average cooling rate in each zone was estimated from the plot. These cooling rate–temperature pairs were then entered into IDS for each corresponding alloy simulation.

The initial material datasets for the nickel based alloys (CW6MC and N3M) were generated using JMatPro.[3]

Table 2 Measured characteristic temperatures during solidification and cooling, along with latent heats

Metal type	Alloy	Event	Temperature/°C	Latent heat/kJ kg^{-1}
Stainless steel	CN3MN	T_{liq}	1387 ± 1	180 ± 10
		$T_{secondary\ phase}$	1380 ± 2	
		T_{sol}	1300 ± 5	
	CD3MN	T_{liq}	1455 ± 2	162 ± 10
		$T_{secondary\ phase}$	1447 ± 3	
		T_{sol}	1385 ± 3	
		$T_{fer\text{-}aus\ start}$	1276 ± 3	
	CD4MCuN	T_{liq}	1450 ± 3	162 ± 10
		$T_{secondary\ phase}$	1437 ± 4	
		T_{sol}	1368 ± 3	
		$T_{fer\text{-}aus\ start}$	1223 ± 2	
Nickel based alloy	CW6MC	T_{liq}	1324 ± 1	179 ± 10
		$T_{secondary\ phase}$	1306 ± 4	
		$T_{tertiary\ phase}$	1210 ± 2	
		T_{sol}	1177 ± 3	
	N3M	T_{liq}	1374 ± 1	158 ± 10
		$T_{secondary\ phase}$	1364 ± 2	
		$T_{tertiary\ phase}$	1284 ± 5	
		T_{sol}	1254 ± 4	
		$T_{solid\ state}$	830 ± 5	

Because JMatPro uses a modified Scheil approximation and does not consider finite rate solute diffusion, cooling rate data are not considered by the program. Because the Scheil approximation is utilised, however, it is necessary to specify a solidification cutoff value. When the liquid fraction reaches the cutoff value, solidification is considered complete. The cutoff values for the nickel based alloys were adjusted until the predicted solidus temperatures matched the measured values. Note that without the present measurements of the solidus temperature, it would not have been possible to determine an accurate cutoff value. For CW6MC, the cutoff value found was 18·3%, and for N3M, the cutoff value was 13·1%. The probable reason for these large cutoff values is that these datasets were generated using the general steel thermodynamic database in JMatPro, which was the most appropriate database available to the present researchers. A more appropriate thermodynamic database, specifically tailored for nickel based alloys, might give smaller cutoff values. It is also possible that the modified Scheil approximation is not appropriate for these alloys.

The initial material datasets produced by the thermodynamic simulation software packages provide temperature dependent values of the density, thermal conductivity, specific heat and kinematic viscosity of each alloy. These datasets also contain a solidification path and a value for the latent heat; however, the final values of these quantities were determined by comparing measured and simulated data, as explained below. In addition, the IDS datasets for the two duplex steels (CD3MN and CD4MCuN) also predict the ferrite to austenite transformation. For both alloys, the predicted ferrite to austenite transformation start temperature was in approximate agreement with the measured values listed in Table 2. The final microstructure predicted for both duplex steels was ~50% ferrite–50% austenite, as expected. No solid state transformation was predicted for CN3MN, which solidifies as austenite and remains austenite down to room temperature.

The liquidus and solidus values predicted by the thermodynamic software packages typically differed by several degrees from the measured values given in Table 2. Because of these discrepancies, small adjustments were made to some of the material datasets for density, thermal conductivity, specific heat and kinematic viscosity of each alloy. This was necessary because particularly at liquidus, sudden changes occur in some of these properties (i.e. if a property is displayed as a function of temperature, such a change would appear as a 'kink' in the property curve). Since the measured liquidus and solidus values were used to generate the solidification paths for these alloys (*see* below), consistency required that these kinks in the property curves occur at the measured temperatures rather than at their simulated counterparts; therefore, the kinks were shifted from the predicted temperatures to the measured values.

The casting experiments were simulated using the general purpose casting simulation software package MAGMASOFT.[16] The rigging shown in Fig. 1 was used for the simulations. For each alloy, virtual TCs were placed in locations corresponding to the actual TC locations in the casting experiments. The numerical grid used $\Delta x=\Delta y=4$ mm and $\Delta z=3{\cdot}2$ mm, resulting in eight computational cells through the plate thickness, and a total of ~214 000 cells in the metal. The mould material used to model the phenolic urethane no bake sand moulds was FURAN from the MAGMASOFT database. For CD3MN, the chromite sand around the plate was modelled with the MAGMASOFT database CR_SAND. The initial sand temperatures for each alloy were determined from the sand TC readings before the mould temperatures began to rise (21–22°C). The IHTC between the metal and the sand mould was taken as a constant value of 1000 W m^{-2} K^{-1}. The legitimacy of this choice will be examined shortly. Filling and solidification were simulated for one plate of each alloy. A simulation fill time of 10 s was selected for all the alloys; the recorded fill times were all between 9 and 11 s, and previous simulation experience indicates that changing the fill time by ± 1 s effects negligible changes in the results.

Superaustenitic stainless steel CN3MN

For each alloy, the corresponding initial material dataset was input into the simulation using the solidification path and latent heat predicted with the dataset as initial estimates of those quantities. As discussed in the section entitled 'Casting simulation input', the simulation pouring temperature T_{pour} was an unknown simulation parameter. Fortunately, it is possible to determine the correct simulation pouring temperature using the following time to liquidus method. Consider CN3MN as an example. Using the initial IDS material dataset, a simulation was performed for plate A. This initial simulation used $T_{pour}=1540$°C as a first guess of the pouring temperature (the furnace temperature recorded for this alloy was 1598°C). The temperature and cooling rate curves resulting from the plate's right virtual TC (TC-R, as shown in Fig. 1*c*) in this simulation are compared with the measured values from plate A (TC-R in Fig. 9*a*). Note that the IDS solidification path used in this simulation has a liquidus temperature of 1°C less than the measured value and a solidus temperature of 2°C less than the measurement (*see* Table 3 below); these small differences are not visible in the temperature scale used in Fig. 9. Both the virtual and real TCs begin to heat at the same time, when metal first comes into contact with them. The virtual TC immediately jumps to the temperature of the surrounding metal, but the real TC has some thermal lag. For $T_{pour}=1540$°C, it is evident in Fig. 9*a* that the virtual TC reaches the measured liquidus temperature (indicated by the upper dashed line) later than the measured TC (by ~15 s). This indicates that the simulation superheat is too high, and thus, T_{pour} is lower than this first guess of 1540°C.

With this information, additional simulations were run with the same material dataset but with different values of T_{pour}. After several iterations, $T_{pour}=1502$°C was selected. The resulting temperature and cooling rate curves for TC-R in this simulation are shown in Fig. 9*b*. With this choice of T_{pour}, the time to reach liquidus in the simulation now agrees with the measurement, indicating that the correct simulation pouring temperature has been determined. Note that this pouring temperature will continue to give the correct time to liquidus as changes are made to the latent heat and solidification path, because the time to liquidus is primarily affected by properties above the liquidus temperature.

While the time to liquidus is now the same for the simulation and measurement in Fig. 9*b*, there is still a large discrepancy between the measured and simulated times to reach the solidus temperature (indicated by the

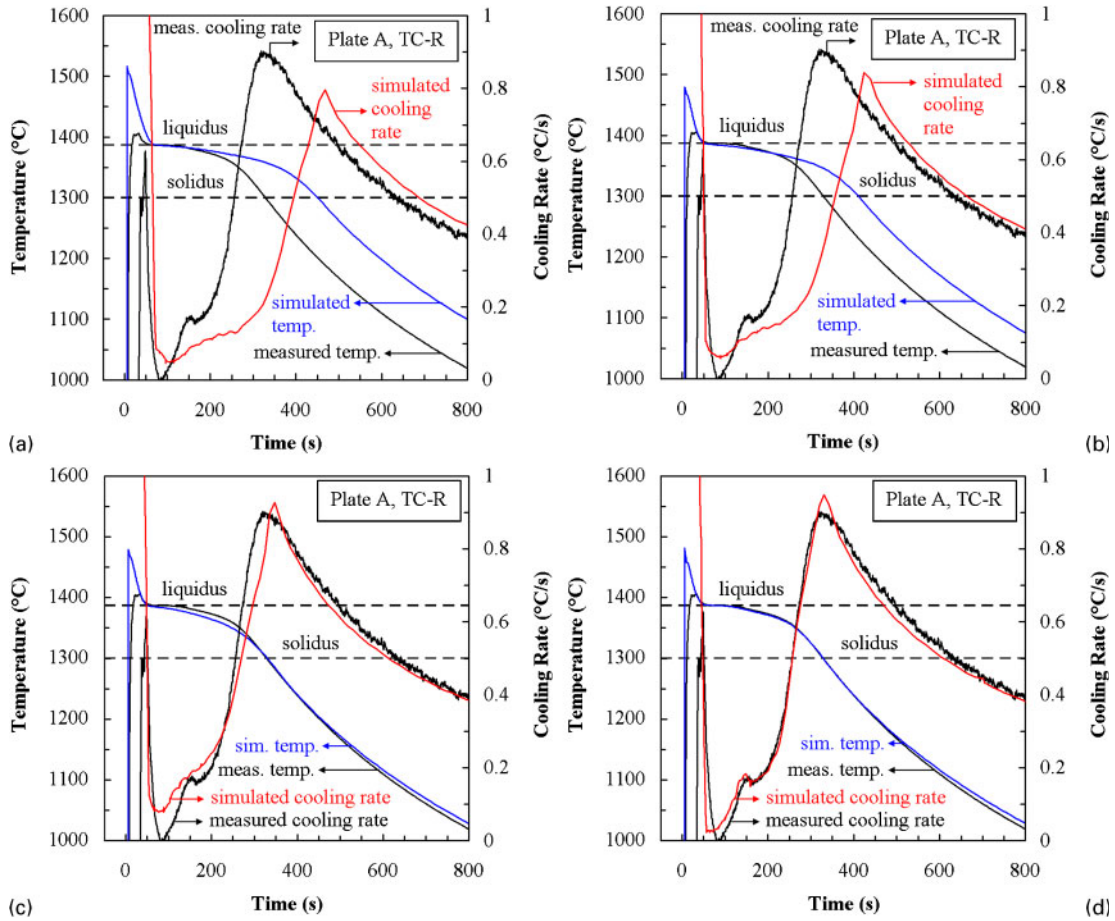

a T_{pour}=1540°C, IDS solidification path and latent heat (L=253 kJ kg^{-1}); *b* T_{pour}=1502°C, IDS solidification path and latent heat (L=253 kJ kg^{-1}); *c* T_{pour}=1502°C, IDS solidification path, L=200 kJ kg^{-1}; *d* T_{pour}=1502°C, modified solidification path, L=180 kJ kg^{-1}

9 Simulated and measured temperatures and cooling rates for CN3MN simulations using different initial metal temperatures and material properties

Table 3 Comparison between solidification ranges and latent heats determined experimentally with corresponding values from thermodynamic simulation software

				Values from simulation software	
Metal type	Alloy	Value	Values determined from experiments	IDS*	JMatPro†
Stainless steel	CN3MN	T_{liq}/°C	1387	1386	1400
		T_{sol}/°C	1300	1298	1246
		L/kJ kg^{-1}	180	252	217
	CD3MN	T_{liq}/°C	1455	1457	1468
		T_{sol}/°C	1385	1378	1380
		L/kJ kg^{-1}	162	178	154
	CD4MCuN	T_{liq}/°C	1450	1436	1428
		T_{sol}/°C	1368	1302	1175
		L/kJ kg^{-1}	162	187	167
Nickel based alloy	CW6MC	T_{liq}/°C	1324	N/A	1331
		T_{sol}/°C	1177	N/A	1065
		L/kJ kg^{-1}	179	N/A	237
	N3M	T_{liq}/°C	1374	N/A	1375
		T_{sol}/°C	1254	N/A	1077
		L/kJ kg^{-1}	158	N/A	160

*IDS results were generated with the stainless steel option in the software using temperature dependent cooling rate profiles determined from experiments. The CD4MCuN copper content (3%Cu) exceeds the IDS range of 0–1%. The CN3MN nickel content (25·07%Ni) exceeds the IDS range of 0–16%, and the CN3MN molybdenum content (6·41%Mo) exceeds the IDS range of 0–4%. Extrapolation errors may occur when IDS ranges are exceeded.
†JMatPro results were generated with the modified Scheil module, utilising a solidification cutoff value of 1%. The stainless steels (CN3MN, CD3MN and CD4MCuN) were modelled with the stainless steel database, and the nickel based alloys (CW6MC and N3M) were modelled with the general steel database.

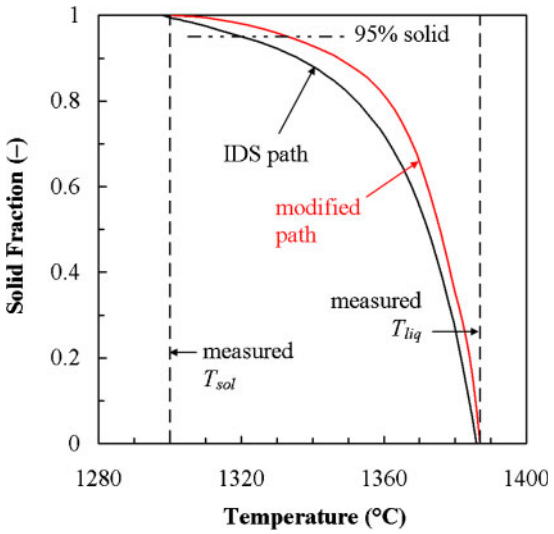

10 CN3MN solidification path generated by IDS compared with modified path determined through analysis of TC data

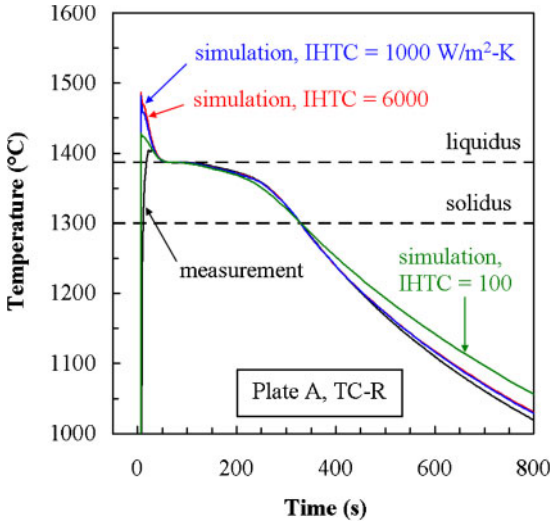

11 Measured CN3MN temperatures compared with simulated values computed with different mould/metal IHTCs

lower dashed line). This large discrepancy exists regardless of the choice for the simulation pouring temperature (*see* Fig. 9*a* and *b*). The simulated time to solidus is much longer than the measured time, indicating that solidification is proceeding too slowly in the simulation. This is largely because the value of latent heat given by IDS for CN3MN (L_f=253 kJ kg^{-1}) is too large. To illustrate how changing the latent heat changes the solidification time, Fig. 9*c* shows the results of a simulation run with T_{pour}=1502°C, but with the latent heat changed to L_f=200 kJ kg^{-1}. This figure demonstrates that changing the latent heat clearly changes the time the simulation takes to reach solidus. Using L_f=200 kJ kg^{-1} with the initial IDS dataset, the time to solidus in the simulation is now the same as the measured time.

Although the simulation times to liquidus and solidus in Fig. 9*c* are now in agreement with the measured values, the simulated and measured temperatures and cooling rates do not agree very well in the solidification range. To bring the temperatures into better agreement during solidification, it is necessary to alter the solidification path. This involves a substantial amount of iteration: adjusting the solidification path, then running a simulation and comparing the new simulation results to the measurements and using this information to make further adjustments to the solidification path. The results from the simulation with the final modified solidification path (*see* Fig. 10) are shown in Fig. 9*d*. Now, the temperatures and cooling rates during solidification are in very good agreement. Note that the latent heat listed in Fig. 9*d* has changed from 200 kJ kg^{-1} (in Fig. 9*c*) to 180 kJ kg^{-1}. This change in the latent heat required to get agreement in the time to solidus is the result of changing the solidification path. The physical explanation for the change in latent heat as the solidification path changes can be understood by considering equation (2): changing the solidification path changes df_s/dT, so in order to obtain the same effective specific heat, the value of the latent heat must change as well. The final latent heat value determined for CN3MN (180 kJ kg^{-1}) is listed in the rightmost column of Table 2. An uncertainty estimate of $\pm$10 kJ kg^{-1} is included with this value. This uncertainty arises primarily due to variations seen when simulating the other plate of the same alloy (not shown here). A discussion of the final latent heat value, together with a comparison to predicted values, can be found in the section entitled 'Comparison between measured values and thermodynamic simulation values'.

It could be fairly stated that the dataset used to generate the results in Fig. 9*c* is already acceptable, without modification of the solidification path. The agreement between measured and simulated temperatures below solidus is essentially the same as the results with the modified solidification path (Fig. 9*d*), and the temperature differences seen in the solidification region in Fig. 9*c* are not overly large. Thus, the overall temperature prediction with the original solidification path would be reasonable. The motivation behind modifying the solidification path lies in casting defect prediction. Many casting defects (solidification shrinkage, hot tears, etc.) occur near the end of solidification. Accurate prediction of these defects requires an accurate representation of the solidification path in this region. The IDS solidification path is compared with the modified path in Fig. 10. The modified path forms solid faster near liquidus and slower near solidus than the IDS path. The horizontal dashed line near the top of this plot indicates the point where the metal is 95% solidified. The IDS solidification path reaches 95% solid 22°C above solidus, whereas the modified path reaches 95% solid 33°C above solidus. This significantly larger temperature difference with the modified path provides more opportunity for defects to form. In other words, using the IDS solidification path may lead to an underprediction of defects compared with the modified path.

Comparing Fig. 9*a* and *d* clearly illustrates that this iterative procedure, wherein modifications to the simulation pouring temperature and to the original dataset are made by comparing measured and simulated TC results and then adjusting the simulated dataset until the results agree, is very effective (if somewhat tedious). To summarise, the present procedure involves the following steps:

(i) beginning with the initial material dataset and a guess for the simulation pouring temperature,

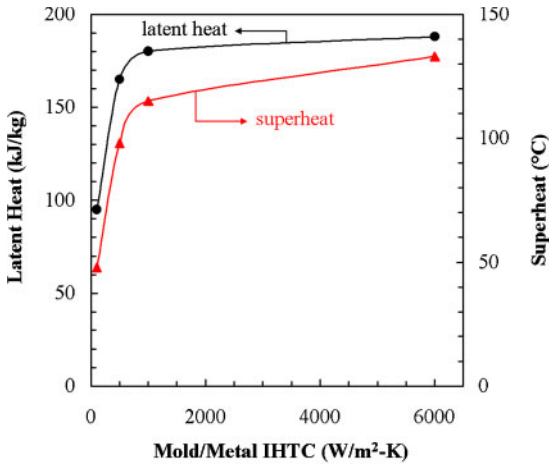

12 Effect of IHTC on superheat and latent heat required to achieve agreement between simulated and measured time required to reach liquidus and solidus temperatures in CN3MN plate A, TC-R

adjust T_{pour} until the simulated and measured times to reach liquidus agree

(ii) adjust L_f until the simulated and measured times to reach solidus agree

(iii) adjust the solidification path (and L_f again, as necessary) until the simulated and measured temperatures and cooling rates during solidification agree.

Parametric study of IHTCs

Before continuing on with the other alloys, the choice of the mould/metal IHTC used in the simulations discussed thus far (taken as a constant of 1000 W m^{-2} K^{-1}) is investigated. Figure 11 shows the measured temperature results (again from CN3MN, plate A, TC-R) along with the corresponding results from three different simulations. The simulations each used a different constant value of IHTC: one is the simulation from Fig. 9*d*, with IHTC =1000 W m^{-2} K^{-1}, one used IHTC=100 W m^{-2} K^{-1} and one used IHTC=6000 W m^{-2} K^{-1}. All three simulations were performed using the modified solidification path shown in Fig. 10. Because the heat transfer from the metal to the mould is different in each of these simulations, even during pouring and initial cooling of the liquid metal, the simulation pouring temperature required to produce the correct time to liquidus is different for each simulation: for IHTC=6000 W m^{-2} K^{-1}, T_{pour}=1520°C; for IHTC =1000 W m^{-2} K^{-1}, T_{pour}=1502°C (as in Fig. 9*d*); and for IHTC=100 W m^{-2} K^{-1}, T_{pour}=1435°C. Similarly, the value of latent heat required to get agreement with the time to solidus is also different for each simulation. The differences in the pouring temperature and latent heat between these simulations are depicted in Fig. 12. The pouring temperature is plotted in a more meaningful form as the superheat (=T_{pour}–T_{liq}, where T_{liq}=1387°C for CN3MN). Data from an additional simulation not shown in Fig. 11, with IHTC=500 W m^{-2} K^{-1}, are included to clarify the nature of the steep drop in the curves shown in Fig. 12. Note that neither the superheat nor the latent heat changes significantly from 1000 to 6000 W m^{-2} K^{-1}, and that both of these quantities drop rapidly below 1000 W m^{-2} K^{-1}. Returning to Fig. 11, it is seen that there is very little difference in the predicted temperature curves for 1000 and for 6000 W m^{-2} K^{-1}, and that both agree well with the measured temperature curve. This implies that any constant IHTC >1000 W m^{-2} K^{-1} will give results very similar to the 1000 W m^{-2} K^{-1} results. Figure 12 indicates that the simulation superheats and latent heats required to obtain agreement with the measurements vary only slightly for IHTCs between 1000 and 6000 W m^{-2} K^{-1}. It also appears from Fig. 11 that 100 W m^{-2} K^{-1} is too small, because the temperature for 100 W m^{-2} K^{-1} decreases too slowly below the solidus temperature. In addition, the superheat and latent heat values shown in Fig. 12 for 100 W m^{-2} K^{-1} are much too small to be realistic.

Further evidence of which IHTC should be used can be found by comparing sand TC measurements. Figure 13 shows the measured and simulated sand TC temperature curves corresponding to the metal temperatures shown in Fig. 11. Figure 13*a* shows the values for TC-U, which was 2·0 in. (5·08 cm) above plate A, and Fig. 13*b* shows the values for TC-D, which was 1·1 in. (2·79 cm) above plate A. As in Fig. 11, the 1000 and 6000 W m^{-2} K^{-1} simulation results are in good agreement

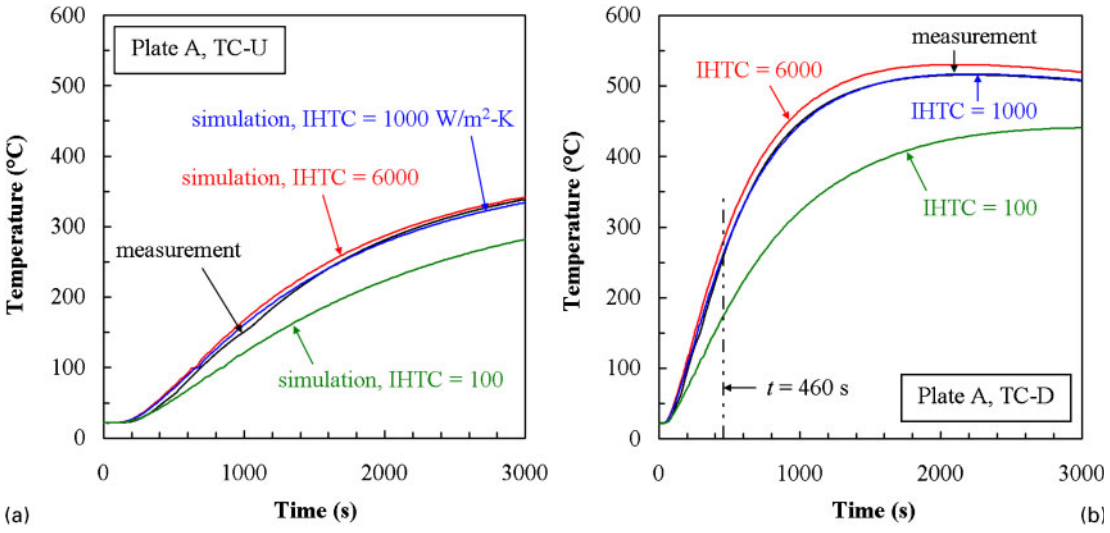

a sand TC 2·0 in. above plate surface; *b* sand TC 1·1 in. above plate surface

13 Measured sand temperatures for CN3MN plate A mould compared with simulated values computed with different IHTCs

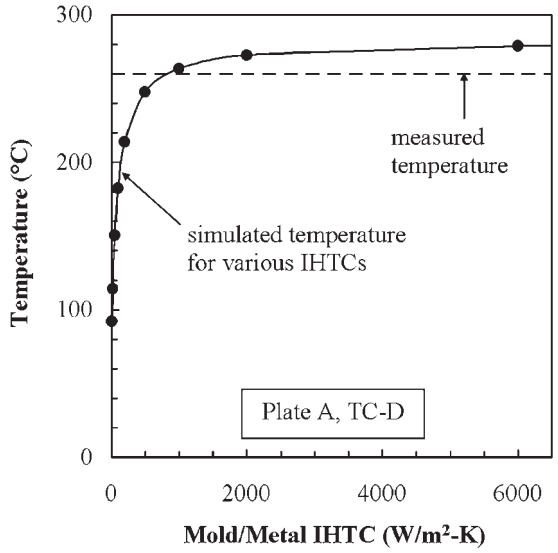

14 Comparison between measured sand temperature at t=460 s for TC-D in CN3MN plate A mould and corresponding simulated temperatures for simulations with various IHTCs

with each other and with the measured temperatures. Figure 13 further indicates that the value of 100 W m^{-2} K^{-1} is too small, since both the TC-U and TC-D temperature measurements are significantly underpredicted using this IHTC.

Finally, the data for TC-D from the plate A mould are further investigated in Fig. 14, which plots the simulation temperatures at time t=460 s as a function of IHTC (this time is indicated as a vertical dashed line in Fig. 13*b*). The measured temperature from TC-D at this time (260°C) is shown as a horizontal dashed line. Using the filling simulation temperature results and final CN3MN material dataset from the base case IHTC =1000 W m^{-2} K^{-1} simulation (i.e. the simulation with T_{pour}=1502°C, L=180 kJ kg^{-1} and the modified solidification path), solidification was simulated with several different values of IHTC. The curve of the simulated data in Fig. 14 shows that the 1000 W m^{-2} K^{-1} result agrees very well with the measured value, and that the IHTC values between 500 and 6000 W m^{-2} K^{-1} give reasonable agreement with the measured sand temperature. Below ~500 W m^{-2} K^{-1}, the predicted sand temperature drops rapidly, indicating that the IHTC is too small. Based on the information in Figs. 11–14, the choice of IHTC=1000 W m^{-2} K^{-1} appears to be quite reasonable, and therefore, this IHTC will continue to be utilised for the other alloys.

The conclusion that IHTC=1000 W m^{-2} K^{-1} gives reasonable results is not surprising; sand casting simulation users at steel foundries commonly use values in the range of 800–1000 W m^{-2} K^{-1}. However, these values were settled on empirically. The present parametric study systematically demonstrates that 1000 W m^{-2} K^{-1} is a reasonable value, and it also shows the sensitivity of the results to the choice of IHTC. One could argue that in reality, the IHTC is a temperature dependent quantity, and that a higher value should be used when the metal is all liquid, for example. While this may be true, a constant IHTC is nonetheless effective because the predicted results are insensitive to the IHTC for values above 1000 W m^{-2} K^{-1}, as demonstrated here. Hence, the value used for the IHTC should no longer be considered as a source of uncertainty for the solidification path and latent heat determination. It should be noted that the present discussion of the IHTC focuses only on metal temperatures down to ~1000°C. It is possible (and true based on the authors' experience) that the IHTC should be lowered as the metal experiences further contractions down to room temperature.

Duplex stainless steels CD3MN and CD4MCuN

Next, the iterative procedure described in the section entitled 'Superaustenitic stainless steel CN3MN' was applied to the two duplex stainless steels (CD3MN and CD4MCuN). Comparisons between measured TC results and corresponding simulation results are shown in Fig. 15 for CD3MN and in Fig. 16 for CD4MCuN. Figures 15*a* and 16*a* show results from simulations that used the original, unmodified IDS datasets, and Figs. 15*b* and 16*b* show results from simulations that used the final modified datasets. All the results in Figs. 15 and 16 were produced using the correct pouring temperature. The final latent heat values determined for these alloys are listed in Table 2. The original IDS dataset simulation results in Fig. 15*a* for CD3MN are in fair agreement with the measurements, but the simulation begins to cool too slowly near the end of solidification, and this trend continues below solidus.

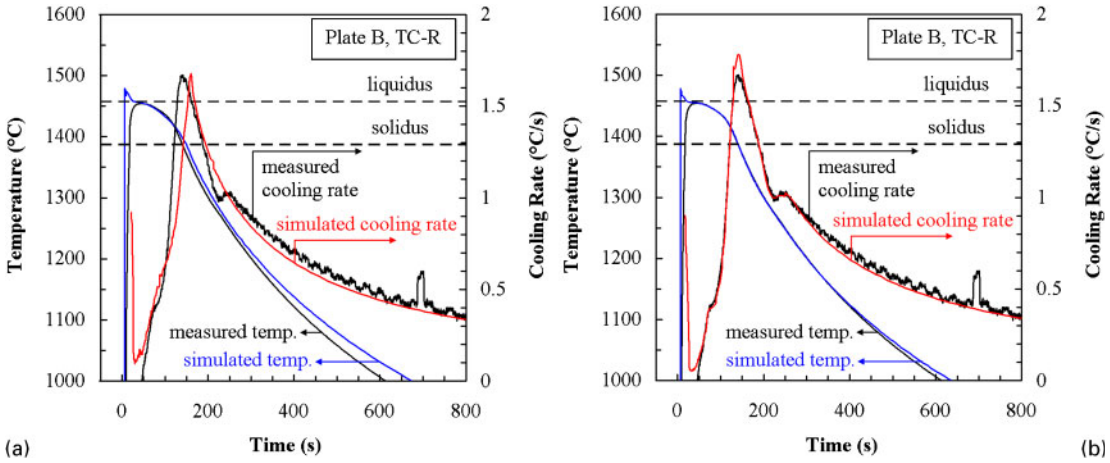

15 Comparison of simulated and measured CD3MN temperatures and cooling rates for plate B, TC-R, using *a* initial IDS dataset and *b* final modified dataset (T_{pour}=1504°C)

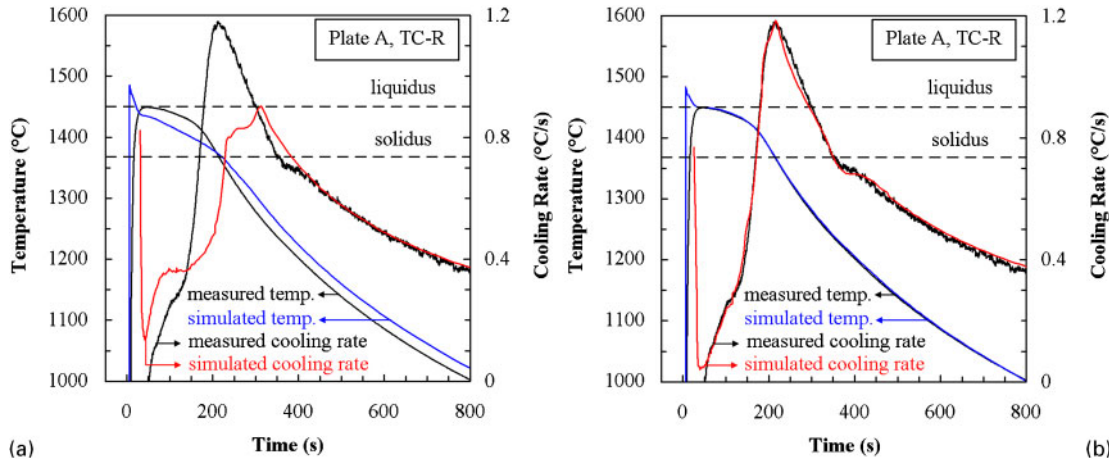

16 Comparison of simulated and measured CD4MCuN temperatures and cooling rates for plate A, TC-R, using *a* initial IDS dataset and *b* final modified dataset (T_{pour}=1508°C)

Excellent agreement between measurement and simulation is seen after the dataset is modified, as shown in Fig. 15*b*. In contrast to CD3MN, Fig. 16*a* shows that the original IDS dataset simulation results for CD4MCuN are in poor agreement with the measured results. The simulation cools too quickly during solidification and then too slowly in subsequent cooling below solidus. The reason that the original dataset for CD3MN gives somewhat reasonable results, while the original dataset for CD4MCuN gives very poor results, is the large copper content in CD4MCuN. The 3%Cu addition exceeds the allowable IDS range for this alloying element, which is 0–1%. In this instance, the extrapolation that IDS performs with the large copper content creates an unrealistic liquidus value and solidification path. Modification of this dataset, however, to correct the solidification range and latent heat, produces excellent agreement between measurement and simulation, as seen in Fig. 16*b*.

For these duplex steels, additional dataset modification was required to produce the 'kinks' seen in the cooling rate curves after solidification is complete, which correspond to the latent heat release during the ferrite to austenite transformation. IDS contains a model that simulates austenite decomposition below 1000°C and accounts for the latent heat related to this transformation; however, although IDS simulates the ferrite to austenite transformation that occurs in these alloys in terms of phase fractions, it does not account for the associated latent heat release. This latent heat release can be added manually to the thermophysical datasets by modifying the specific heat curve. The modified specific heat curves for the duplex steels are shown in Fig. 17 along with the corresponding original IDS specific heat curves. The modified specific heat curves each have a spike, whose peak occurs at the ferrite to austenite transition start temperature listed in Table 2. The height of the spikes, and the width of their bases, was determined through the same type of procedure that has been discussed throughout this paper, changing the shape until the simulated cooling rate curves matched the measured values. The spikes seen in the IDS specific heat curves in Fig. 17 are the result of the IDS austenite decomposition model. Even though IDS correctly predicts the phase fractions of ferrite and austenite during the ferrite to austenite transformation, the spike that corresponds to austenite decomposition, peaking at ~600°C, still appears in the specific heat curves. This spike was removed in the modified curves since austenite decomposition does not occur. The slope of the modified

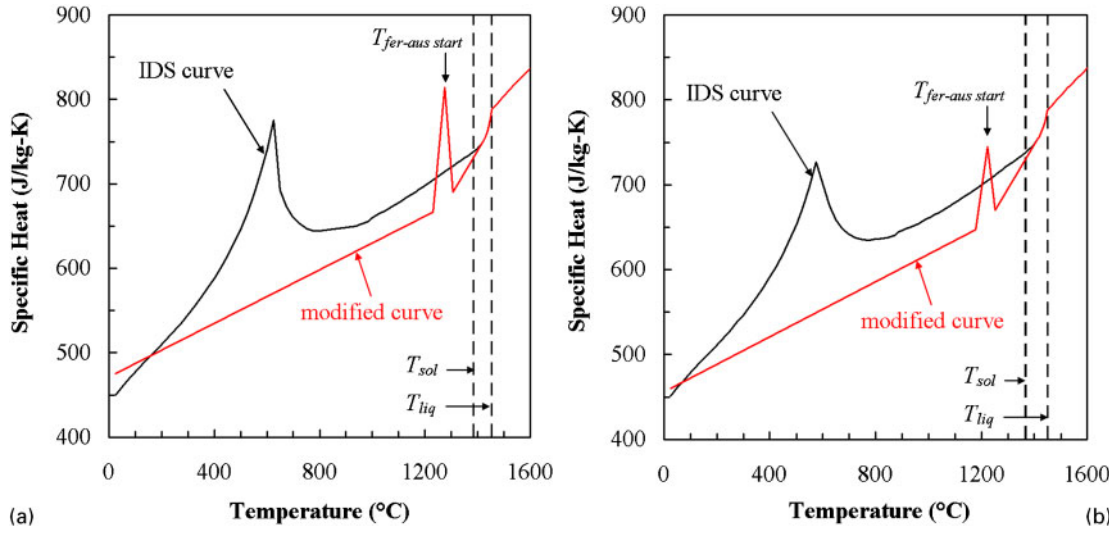

a CD3MN; *b* CD4MCuN

17 Comparison between original IDS and modified specific heat curves for duplex stainless steels

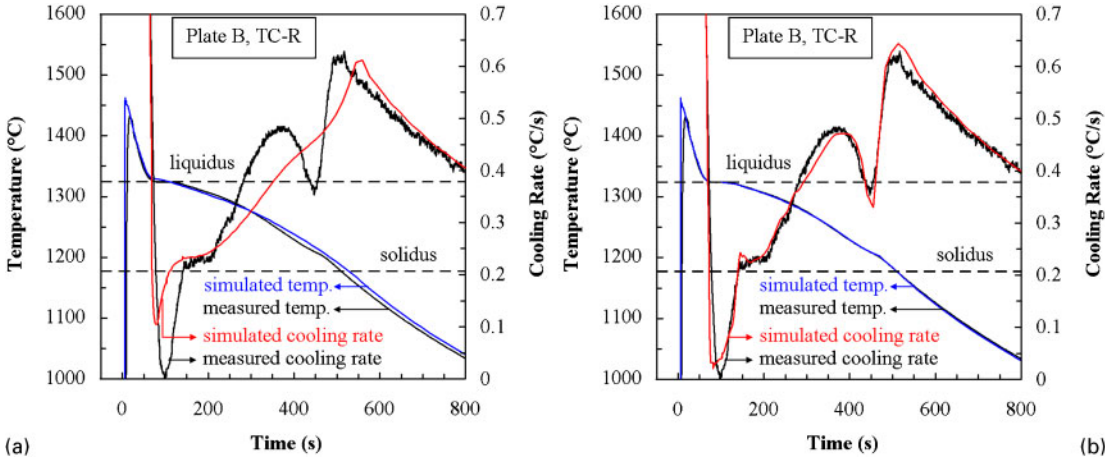

18 Comparison of simulated and measured CW6MC temperatures and cooling rates for plate B, TC-R, using *a* initial JMatPro dataset and *b* final modified dataset (T_{pour}=1486°C)

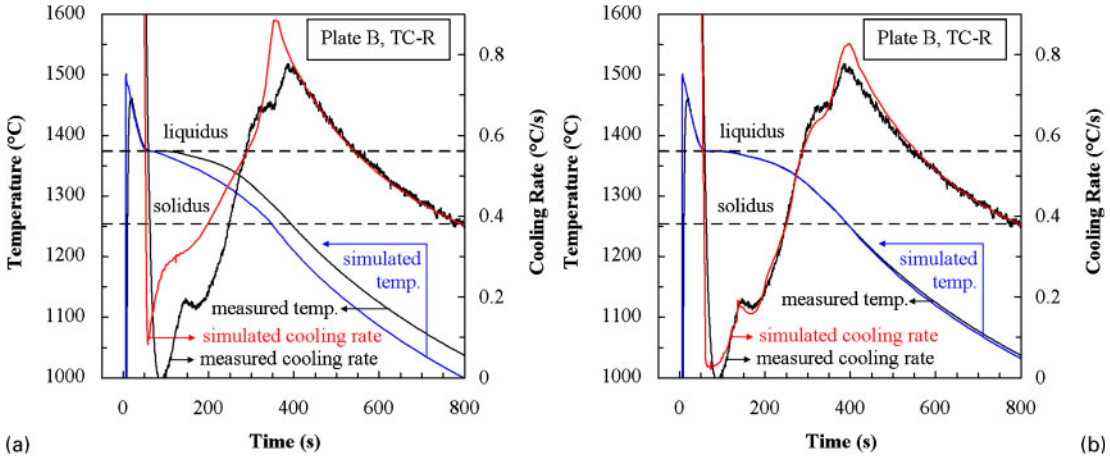

19 Comparison of simulated and measured N3M temperatures and cooling rates for plate B, TC-R, using *a* initial JMatPro dataset and *b* final modified dataset (T_{pour}=1528°C)

curves after the ferrite to austenite spike was chosen to match the slope of the IDS curves just below solidus. The decrease in the modified specific heat curves compared with the IDS curves that begins near the end of solidification was determined again through an iterative manner. Figures 15*b* and 16*b* show that the modified specific heat curves give good agreement between measurement and simulation below solidus. Although it is not shown in Figs. 15*b* and 16*b*, reasonable agreement between simulation and measurement is seen down to ~600°C (where temperature measurement ended), indicating that removal of the peak in the IDS curves is valid.

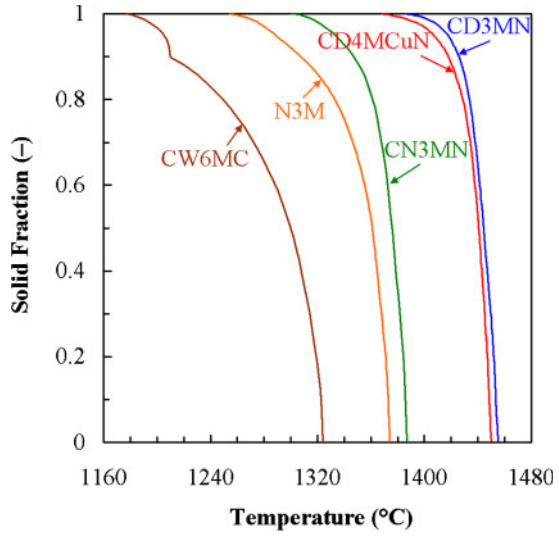

20 Final solidification paths determined for five alloys in present study

Nickel based alloys CW6MC and N3M

Finally, the iterative procedure was applied to the two nickel based alloys (CW6MC and N3M). The TC comparison results for both the unmodified JMatPro dataset simulations and the modified dataset simulations are given in Fig. 18 for CW6MC and in Fig. 19 for N3M. Again, the final latent heat values found for these alloys are listed in Table 2. The simulated temperature results for CW6MC with the original JMatPro dataset, shown in Fig. 18*a*, are in relatively good agreement with the measurements. However, comparison between measured and simulated cooling rate curves in the solidification range shows poor agreement. The simulated cooling rate curve only approximately captures the secondary solid phase formation that occurs at ~150 s and entirely misses the sharp local minimum due to the tertiary phase

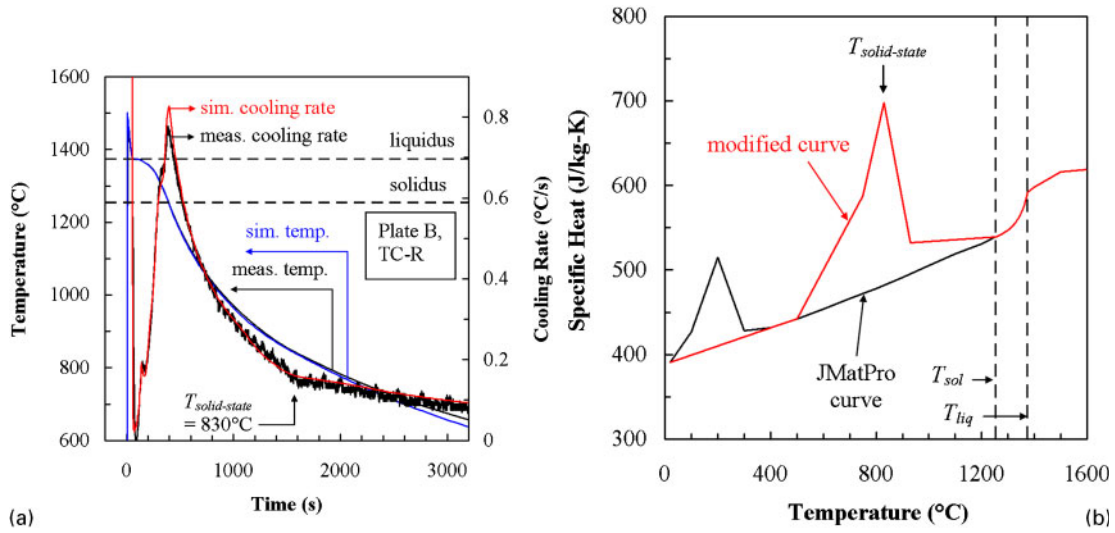

21 ***a*** **N3M results from Fig. 19, shown over longer time span to include solid state transformation and** ***b*** **N3M original and modified specific heat curves**

formation at ~450 s. Once the CW6MC dataset is modified, however, Fig. 18*b* shows that both simulated temperature and cooling rate curves give excellent agreement with the measurements. In order to capture the large spike (local minimum) in the cooling rate curve associated with the tertiary phase formation, it was necessary to put a significant kink in the CW6MC solidification path. The final solidification path for CW6MC is shown in Fig. 20 along with the final solidification paths determined for the other alloys.

The original JMatPro dataset simulation results for N3M, shown in Fig. 19*a*, do not agree well with the measured temperatures or cooling rates. The simulated casting cools too fast in the solidification region. The secondary solid phase is again only very approximately modelled by an inflection in the cooling rate curve, and the tertiary solid phase is completely missed. The modified dataset simulation results, shown in Fig. 19*b*, again show excellent agreement with the measured values.

Finally, the N3M simulation results shown in Fig. 19*b* are repeated in Fig. 21*a*, showing a larger temperature range and time scale. As with the duplex steels, an additional modification had to be made to the specific heat curve for N3M in order to account for a solid state transformation that can be seen by the kink in the measured cooling rate curve for N3M at ~830°C in Fig. 21*a*. This transformation (whose value is included in Table 2) is not shown in Fig. 8 because the temperature range in Figs. 4–8 (1000–1500°C) was selected to highlight the solidification ranges. The N3M solid state transformation is the only transformation that is not shown in Figs. 4–8. To model this transformation, the N3M specific heat curve was modified below solidus, as shown in Fig. 21*b*. The modification to the original JMatPro curve was again determined iteratively. Note that the JMatPro curve has a peak similar in shape to the modified peak but occurring at a much lower temperature. It is possible that the JMatPro peak accounts for the same transformation the modified peak is capturing, just over a temperature range that is too low. With this modified specific heat curve, Fig. 21*a* shows that the simulated temperature and cooling rate curves are in excellent agreement with the measurements.

Comparison between measured values and thermodynamic simulation values

In an effort to lend further credence to the values provided in Table 2, Table 3 compares the measured liquidus, solidus and latent heat values with the corresponding values predicted by IDS and JMatPro. The IDS results were generated using the stainless steel option in the software, with cooling rate profiles determined from the experiments. Recall that the CD4MCuN copper content (3%Cu) exceeds the IDS range of 0–1%. In addition, the CN3MN nickel content (25·07%Ni) exceeds the IDS range of 0–16%, and the CN3MN molybdenum content (6·41%Mo) exceeds the IDS range of 0–4%. IDS cannot be used for the two nickel based alloys. The JMatPro results were generated assuming a default solidification cutoff value of 1%. The stainless steels (CN3MN, CD3MN and CD4MCuN) were modelled with the JMatPro stainless steel database, and the nickel based alloys (CW6MC and N3M) were modelled with the general steel database.

First, compare the measured and simulated liquidus values. IDS gives liquidus temperatures very close to the measured values for CN3MN (different by 1°C) and CD3MN (different by 2°C), which instils confidence in the measured values for these steels. There is a large discrepancy between the IDS value and the measured liquidus value for CD4MCuN (different by 14°C), which is due to extrapolation errors in IDS resulting from the large copper content of this alloy. The reason that extrapolation errors are assumed for this alloy can be seen by comparing the compositions of CD3MN and CD4MCuN in Table 1: the compositions are similar, except for the 3% copper content in CD4MCuN. Note the relatively large difference between the IDS and JMatPro predictions for the liquidus values of steels: the two predictions differ by 14°C for CN3MN, by 11°C for CD3MN and by 8°C for CD4MCuN. For the nickel based alloys, reasonable agreement is seen between the JMatPro liquidus predictions and the measured values: the measured and predicted liquidus values differ by 7°C for CW6MC and by only 1°C for N3M.

As with the liquidus temperatures, the measured solidus temperatures and the IDS predictions of these

temperatures are in good agreement for CN3MN (different by 2°C) and for CD3MN (different by 7°C). The difference is very large for CD4MCuN (different by 66°C), but again, this is presumably due to extrapolation errors due to the large copper content. The JMatPro solidus predictions are too low compared with the measurements for all alloys, but this is meaningless; it is due to the small solidification cutoff value of 1% that was used to generate the results for all alloys in Table 3.

Next, compare the measured and predicted values of latent heat. The latent heat predictions by IDS and JMatPro are very weak functions of the liquidus and solidus temperatures, so the validity of the latent heat prediction is not affected by whether or not the freezing range was reasonably predicted for an alloy. Notice that the measured values for CD3MN, CD4MCuN and N3M are all in reasonable agreement with the predicted values. For CD3MN, the measured value (162 kJ kg^{-1}) lies between the two predicted values (178 and 154 kJ kg^{-1}). For CD4MCuN, the measured value (162 kJ kg^{-1}) is noticeably below the IDS value (187 kJ kg^{-1}), but close to the JMatPro value (167 kJ kg^{-1}). In addition for N3M, the measured and predicted values are very close, only differing by 2 kJ kg^{-1}. The discrepancy for CW6MC between the measured value (179 kJ kg^{-1}) and the JMatPro prediction (237 kJ kg^{-1}) can be explained by the fact that JMatPro does not predict the formation of the tertiary phase that forms toward the end of solidification, which causes a significant drop in the cooling rate curve in Fig. 18. Notice that the results in Fig. 18*a*, which were generated using the original JMatPro solidification path and $L=237$ kJ kg^{-1}, show poor agreement in the cooling rate curves near the end of solidification (although the time to solidus is reasonably predicted), while the results in Fig. 18*b*, which were generated using the modified solidification path shown in Fig. 20 with $L=179$ kJ kg^{-1}, correctly predict the sharp decrease in cooling rate due to this tertiary phase. Finally, note the significant discrepancy between the measured and predicted latent heat values for CN3MN. The IDS value of 252 kJ kg^{-1} is too large; the error presumably results from the high nickel content of this alloy significantly exceeding the IDS range. This conclusion is supported by the JMatPro prediction (217 kJ kg^{-1}), which is much lower than the IDS prediction. The JMatPro prediction is still higher than the measured value of 180 kJ kg^{-1}, but this predicted value may also be errantly large. Because reasonable agreement is seen between the measured and predicted latent heat values in CD3MN, CD4MCuN and N3M, and the differences in the values for CW6MC are caused by the failure of the software to predict a significant phase, it seems unlikely that the measured value for CN3MN is significantly errant in only this one alloy.

Conclusions

In the present study, alloy material databases, necessary to perform casting simulations, were developed for five commonly used corrosion resistant alloys: superaustenitic stainless steel CN3MN, duplex stainless steels CD3MN and CD4MCuN and nickel based alloys CW6MC and N3M. Initial material datasets were generated using thermodynamic simulation software. Owing to limitations of the software, however, modifications to these datasets were necessary. The modifications were made utilising temperature measurements taken in each alloy during casting of 1 in. (2·54 cm) thick plates. This thickness, which commonly occurs in castings produced with these alloys, was selected because the solidification path is a function of cooling rate, and it was deemed important to measure the temperatures in a setting that provided cooling rates seen in foundry production of these alloys. Each initial material dataset was then modified using an iterative method, which utilises comparison between measured temperature and cooling rate data with corresponding simulated values to direct changes in the dataset, until satisfactory agreement between simulated and measured temperatures and cooling rates was reached. Primarily, this involved changing the predicted latent heat and the solidification path of all the alloys. It was also necessary to modify the effective specific heat curves for CD3MN, CD4MCuN and N3M in order to correctly account for solid state transformations in these alloys. Uncertainties in the simulation due to unknown pouring temperatures and IHTCs were effectively eliminated through parametric studies and comparisons with measured mould temperatures. The final material datasets developed in this study produce very good agreement between simulated and measured temperatures and cooling curves. Although the present iterative method to determine the solid fraction–temperature relation and latent heat is somewhat tedious, it is believed to be more accurate than traditional Newtonian and Fourier CCA methods that involve small cup castings and the construction of a zero curve.

Acknowledgements

This work was performed with the financial support of the Materials Technology Institute (MTI). However, any opinions, findings, conclusions or recommendations expressed herein are those of the authors and do not necessarily reflect the views of MTI. We are indebted to M. Blair and R. Monroe (of the Steel Founders' Society of America) and to G. Hodge (of MTI) for their input and assistance in the organisation of this project. Most importantly, we thank the employees at Stainless Foundry & Engineering, Inc., for performing the plate casting experiments. This work could not have been accomplished without their shared efforts. In particular, we are very grateful to R. Bird and J. Wagner of Stainless Foundry & Engineering, Inc., for their efforts in pouring the castings.

References

1. J. Miettinen: *Metall. Trans. B*, 1997, **28B**, 281–297.
2. J. Miettinen and S. Louhenkilpi: *Metall. Trans. B*, 1994, **25B**, 909–916.
3. JMatPro v4·0, Sente Software Ltd, Surrey Technology Centre, Surrey, UK.
4. W. J. Boettinger, U. R. Kattner, K. W. Moon and J. H. Perepezko: 'DTA and heat-flux DSC measurements of alloy melting and freezing', 'NIST recommended practice guide', NIST special publication 960-15, Washington, DC, USA, 2006.
5. D. M. Stefanescu, G. Upadhya and D. Bandyopadhyay: *Metall. Trans. A*, 1990, **21A**, 997–1005.
6. E. Fras, W. Kapturkiewicz, A. Burbielko and H. F. Lopez: *AFS Trans.*, 1993, **101**, 505–511.
7. J. O. Barlow and D. M. Stefanescu: *AFS Trans.*, 1997, **105**, 349–354.
8. D. Emadi and L. V. Whiting: *AFS Trans.*, 2002, **110**, 285–296.
9. W. T. Kierkus and J. H. Sokolowski: *AFS Trans.*, 1999, **107**, 161–167.

10. D. Emadi, L. V. Whiting, S. Nafisi and R. Ghomashchi: *J. Therm. Anal. Calorim.*, 2005, **81**, 235–242.
11. 'A guide to the solidification of steels', Jernkontoret, Stockholm, Sweden, 1977.
12. Personal Daq/3005, Measurement Computing Corporation, Norton, MA, USA.
13. DASYLab v8·0, Adept Scientific, Amor Way, Letchworth, Hertfordshire, UK.
14. K. D. Carlson, S. Ou and C. Beckermann: *Metall. Mater. Trans. B*, 2005, **36B**, 843–856.
15. Nanmac Corp., Framingham, MA, USA.
16. MAGMASOFT v4·6, MAGMA GmbH, Aachen, Germany.